Experimental study on the behavior of wear resistant steels under high velocity single particle impacts

Matti Lindroos[1]*, Marian Apostol[1], Veli-Tapani Kuokkala[1], Anssi Laukkanen[2], Kati Valtonen[1], Kenneth Holmberg[2], Olli Oja[3]

[1] Tampere Wear Center, Department of Materials Science, Tampere University of Technology, P.O. Box 589, FI-33101 Tampere, Finland
[2] VTT Technical Research Centre of Finland, P.O. Box 1000, FI-02044 VTT Espoo, Finland
[3] Ruukki Metals Inc. P.O. Box 93, 92101, Raahe, Finland
*Corresponding author: matti.v.lindroos@tut.fi
+358 401981982

Abstract

High velocity solid particle erosion may cause severe damage and high wear rates in materials used for wear protection. An experimental work on the behavior of wear resistant steels, including three high-strength martensitic alloys and a carbide-reinforced metal matrix composite, was performed in high rate single impact conditions. Characterization of the mechanical behavior of the materials at high strain rates was conducted using the Hopkinson Split Bar technique to identify the effects of strain rate on strain hardening and the prevailing failure mechanisms. The high velocity impact experiments using spherical projectiles were carried out at various impact angles and projectile velocities. The effects of impact energy and impact angle were studied and discussed. Wear was analyzed as volume loss from the surface, but it was also presented in a more precise way by taking into account the actual energy spent on the plastic deformation and wear. In-situ high speed photography and post impact characterization of the impact craters were used to reveal the prevailing failure and wear mechanisms. Depending on the impact angle and impact energy, different wear mechanisms of plastic deformation, cutting, shear banding and fracture were identified. The martensitic steels exhibited adiabatic shear banding in the microstructure at high strain rates and impact velocities, which may accelerate the wear. The carbide reinforced steel was found susceptible to catastrophic fracturing especially at high impact angles.

1) Introduction

In the mining industry, protection of machinery against wear is a challenging task due to the harsh loading conditions. Materials are exposed to both heavy abrasion and high energy impacts when, for example, large amounts of rock material is handled, crushed and transported. From the economical point of view, high wear rates or even premature failure of the machinery can become very costly. Also the environmental aspects are becoming more and more important, and therefore materials that can better resist various types of wear are needed. In heavy industrial components, the capability to bear the high traction loads occurring during scratching and the capability to absorb energy during solid particle erosion are of primary importance. The stress states produced by the different loading types, however, have a different dynamic nature, which is a great challenge for most materials. The

use of coatings and composites has in many cases proven useful, but when heavy impacts are considered, steels are still the most widely used materials in wear-prone applications. Lighter structures can be achieved for example by reducing the component wall thicknesses, but to withstand heavy loadings and to retain the component functionality, materials with improved mechanical properties must be developed. In fact, some newly developed high strength steels have in the laboratory scale [1] been shown to provide excellent properties against impact-abrasion type loadings. It is, however, also important to understand their behavior under solid particle erosion and abrasive conditions in order to improve them further.

The theoretical background of solid particle erosion is summarized in various monographs and text books from many different perspectives, including contact mechanics by Johnson [2] and Engel [3], wear and microstructure by Zum-Gahr [4] and Levy [5], and wear testing by Kleis and Kulu [6]. The dynamic nature of impacts exposes the material to high rate deformation, where also inertia effects are considerably affecting the material behavior. Dislocation motion during deformation is a rate dependent property of the microstructure, but also the additional thermal effects have to be accounted for. For example, failure mechanisms that are not observed at quasi-static strain rates may be activated during impacts due to deformation induced heating and nucleation of fracture from defects. The regions subjected to high rate shear deformation may also undergo localization to thin shear bands, known as adiabatic shear banding (ASB) [7]. The ASBs have been reported to be responsible for example for fragmentation [8], damage [9,10] and ballistic failure [11,12] in metallic materials. In high strength steels the adiabatic shear bands are generally divided into deformation shear bands and transformation bands. The transformation bands are also known as white etch bands due to their particular white appearance when etched. The white shear bands have been disputed over the years as to what is their microstructural evolution during loading. According to Dodd and Bai [13], the deformed bands can act as precursors for the harder transformed bands, in which the fractures tend to initiate. What is especially important for the wear behavior of the currently investigated steels is whether or not they exhibit strain rate dependent formation of adiabatic shear bands that can act as precursors for damage and fracture.

In an oblique angle impact, energy is consumed in directions both normal and parallel to the surface. The large shear deformations occurring near the surface region result from the parallel stress component, while compressive deformations result from the normal direction component. Hence the material is required to withstand different stress states that occur depending on the impact direction, friction, and the particle properties. Initially Finnie [14] and Bitter [15,16] proposed a model that has been modified over the years for different purposes in the analytical and numerical models for erosion [17]. Most models accept that wear is related to the energy consumed in the cutting and plastic deformation of the material. The impingement angle [18] has been observed to have a great effect on the erosion rate, which is clearly related to the energy dissipation and failure mechanisms. To properly understand the varying behavior of materials under erosion [19], the exact wear mechanisms and their relation to the failure mechanisms need to be studied in more detail.

In the current work, solid particle erosion was studied with a novel high velocity particle impactor (HVPI) device [20]. The main aim of the work was to elucidate the high strain rate response of high strength steels to oblique impacts in a controlled environment.

2) Materials and methods

The studied materials comprise three commercial hot-rolled wear resistant high strength low alloy (HSLA) plate steels and one carbide reinforced wear resistant steel. One of the HSLA steels is commonly used in abrasion applications, in this paper referred to as Abrasion Resistant Steel

(ABRS). The second one, Impact Resistant Steel (IRS), is typically used in impact wear related applications. The third one is a higher strength still laboratory grade steel intended for similar applications, here referred to as Advanced Impact Resistant Steel (AIRS). Table 1 shows typical as-received macrohardness values for the studied steels. Table 2 presents the nominal compositions and Figure 1 the etched microstructures of the steels. Regardless of the similar surface hardness of the tempered martensitic steels, they have different amounts of untempered martensite in the microstructure, appearing white in the etched micrographs, which increases the strength but can be expected to reduce the toughness. Similarly, the effect of martensite morphology and its high angle boundaries affect the mobility of dislocations, which very likely affects the strength and failure properties of the steels. The AIRS has the finest grain size, whereas ABRS and IRS have larger grain sizes but different amounts and distributions of untempered martensite.

For a comparison, a high strength chromium carbide (Cr_7C_3) reinforced steel, the 'composite steel' (COMP), was investigated for its suitability for impact conditions. The reinforcing particles are known to increase the abrasion resistance, but they may also increase the susceptibility to crack initiation from stress concentrations in the microstructure, which could result in a low service lifetime in high energy impact conditions.

Table 1. The studied wear resistant steels and their sample sizes in mechanical tests

Material designation	Microstructure	Surface hardness (HV10)	Compression sample size in mechanical testing
ABRS	Tempered martensite (Hot rolled)	500-510	d = 6mm, L0 = 5mm, L0/d = 0.83
IRS	Tempered martensite (Hot rolled)	490-515	d = 6mm, L0 = 7mm, L0/d = 1.17
AIRS	Tempered martensite (Hot rolled)	540-565	d = 6mm, L0 = 6mm, L0/d = 1.0
COMP	Chromium carbides & martensitic matrix	740-760	d = 5mm, L0 = 6mm, L0/d = 1.2

Table 2. Nominal compositions of the wear resistant steels

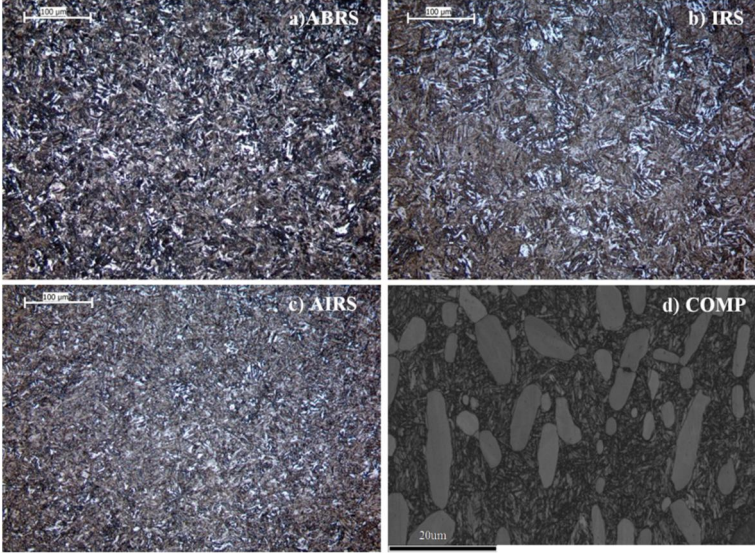| Material	ABRS	IRS	AIRS	COMP
C [%]	0.30	0.32	0.36	2.00
Si [%]	0.80	0.70	0.60	n/a
Mn [%]	1.70	1.50	1.00	n/a
P [%]	0.025	0.015	0.015	n/a
S [%]	0.015	0.005	0.005	n/a
Cr [%]	1.50	1.00	1.50	20.0
Ni [%]	-	2.00	2.50	n/a
Mo [%]	0.50	0.70	0.80	n/a
B [%]	0.005	0.005	0.005	n/a

Figure 1. Microstructures of the studied steels.

2.1 Low and high strain rate mechanical testing

The mechanical testing at low strain rates was performed with an Instron 8800 servohydraulic materials testing machine. All tests were carried out at room temperature using strain rates from 10^{-3} to 10^{0} 1/s. The sample dimensions are presented in Table 1. A thin layer of MoS_2 grease (Molycote) was placed between the tungsten carbide hard metal compression platens and the sample to minimize friction. All mechanical testing on the HSLA steels was performed perpendicular to the rolling plane of the plate. The diameter of the samples was selected based on the strength of the materials and the capacity of the testing machine. The length-to-diameter ratio of all specimens was close to one (see Table 1).

The dynamic properties of the test materials were determined using the compressive Hopkinson Split Bar technique at strain rates ranging from 700 to 3600 1/s. Detailed descriptions of the HSB devices and techniques used at DMS/TUT can be found for example in [21]. The set-up used in this work consisted of 22 mm diameter maraging incident, transmitted and striker bars. High strength steel inserts were placed on both sides of the actual cylindrical sample to prevent deformation and damaging of the incident and transmitted bar ends. The three millimeter thick inserts were changed after every test. To reduce friction and thus the possibility of barreling of the sample, a thin layer of MoS_2 was used between the sample and the inserts. Copper pulse shapers were placed between the striker and the incident bar to smoothen the incident pulse. As usual, the stress, strain and strain rate in the sample were calculated from the three measured stress pulses (i.e., incident, reflected and transmitted pulses) using Equation 1. For the pulses, a dispersion correction was applied following the method originally presented by Gorham [22].

$$\sigma_E(t) = \frac{A_b E \varepsilon_T(t)}{A_s} , \varepsilon_E(t) = \frac{2C_0}{L_s} \int_o^t \varepsilon_R(t) \, dt , \dot{\varepsilon}(t) = \frac{2C_0 \varepsilon_R(t)}{L_s} \tag{1}$$

In Eqn. 1, A_b, E, C_0 are the cross-sectional area, Young's modulus, and the speed of sound in the bar material, A_s, L_s are the cross-sectional area and the gauge length of the sample, ε_T and ε_R are the transmitted and reflected stress pulses, and t is time (note: in cases where dynamic equilibrium of stress in the specimen can be assumed, the calculations can be based on the reflected and transmitted pulses only, as in Eqn. 1). The common logarithmic true stress and true strain equations

were adopted, i.e., $\sigma_T = \sigma_E(1 + \varepsilon_e)$ and $\varepsilon_T = \ln(1 + \varepsilon_e)$.

2.2 High velocity impact testing

To study the impact behavior of the test materials in detail, a new device was developed for the purpose. In this Section, the testing equipment, the test parameters, and the analysis methods used in the tests are described.

2.2.1 HVPI test setup

The high velocity impact experiments were performed with an in-house built equipment, the High Velocity Particle Impactor (HVPI). The authors have previously studied a variety of different sample materials and projectiles using this device, for example in the work of Apostol et al. [20] and Sarlin et al. [23] The equipment, shown in Fig 2, comprises a pressure reservoir and a smooth bore barrel that accelerates the projectile to the target velocity. The distance between the barrel end and the target is typically 1 m. The incident velocity is measured by a commercial chronometer in front of the actual target assembly, which allows the calculation of the projectile's initial kinetic energy prior to the impact. The sample can be fixed at various angles ranging from 0 to 90 degrees (or usually between 10-80 deg). For this particular study, three specific angles were chosen, i.e., 15°±1°, 30°±1° and 60°±1°. The impact event was recorded with a high speed camera (NAC Memrecam fx K5, NAC Image Technology) to analyze the material behavior during the impact. A typical impact incident is shown in Fig 2. In addition to the three impact angles, four different impact energies ranging from 6J to 37J were included in this study.
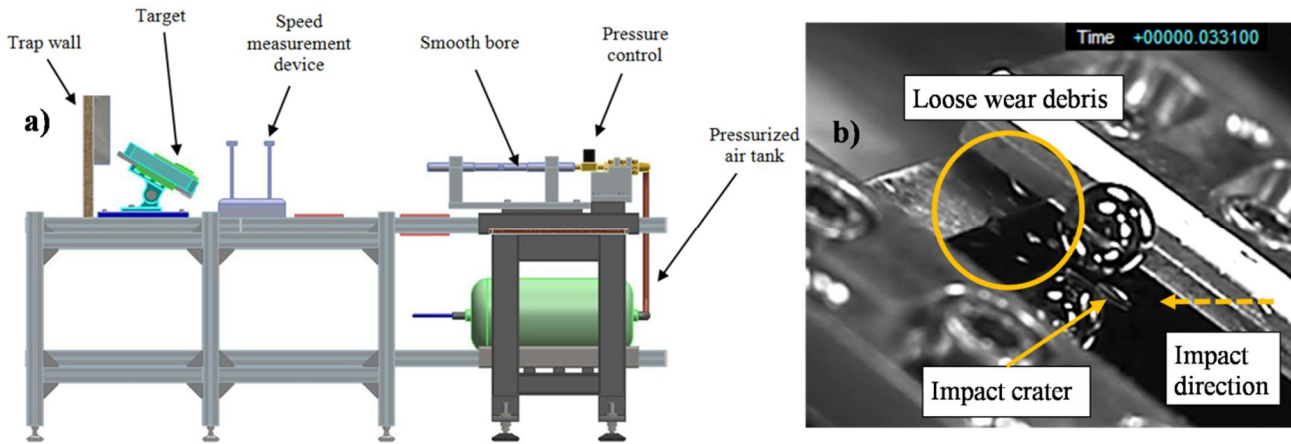

Figure 2. a) High velocity particle impactor [20], and b) a typical high speed impact event.

In the current experiments, spherical WC-Co hard metal projectiles were used. When using this projectile material, the effects of impact particle fragmentation to the surface damage [24] or the wear of the ball do not need to be considered. The diameter of the ball was chosen as 9 mm (grade 10, ISO 3290 [25]), which in general is much larger than usually used in erosion tests (i.e., 200-800 um). This allows tracking of the ball during the impact with a high speed camera system. In addition, a higher amount of energy is transferred to the sample, and thus the deformed volume becomes greater, making the analysis of the erosion craters by optical means easier.

A piezo-electric force sensor was placed below the sample to record the impact forces in three orthogonal directions. During the impact, only a compressive normal force and a tangential sliding force were detected, which was expected since the sensor was located exactly below the impact site. This allows comparison of the actual impact forces in experiments conducted with different angle

settings.

The samples were 40 x 40 mm square plates with a thickness of 5-7 mm depending on the bulk thickness of the available steel plate. The decarburized layer, which easily forms during manufacturing on the surface of ABRS, IRS, AIRS samples, was removed by grinding. The surface finishing was done by polishing with a 1 µm cloth for all materials.

2.2.2 Energy calculations

The dissipated kinetic energy during the impact was calculated by comparing the initial and the residual or reflected kinetic energy of the projectile after the impact. An estimate for the reflected velocity of the projectile was determined from the high speed camera images. The dissipated energy E_d can then be written as

$$E_d = \frac{1}{2} m_p (v_i - v_r)^2 \tag{2}$$

where m_p, v_i, v_r are the projectile's mass, the initial velocity measured in front of the sample, and the reflected velocity determined from the high speed camera images. A special image analysis code was written to overlay the chosen post-impact images and to calculate the residual kinetic energy.

2.3 Material characterization techniques

The samples from mechanical testing were studied and analyzed using an optical microscope before and after etching. The samples were prepared using conventional methods, including cutting, grinding, mounting in resin, and polishing. Basically the same procedure was used to analyze the impact craters and specimen cross-sections after the impact experiments.

The macroscopic hardness of the samples was measured with Struers Duramin-A300 HV5, and the microhardness values from the cross-sections were obtained with a Matsuzawa MMT-7X microhardness tester. Indentations in the shear bands and the white etch surface layers were done using small weight Vickers measurements (HV0.025).

The surface topologies of the impact craters were analyzed using a Plµ confocal imaging profilometer at the VTT Research Center of Finland, and a Wyko NT-1100 optical profilometer at Tampere Wear Center. A special Matlab code was developed to analyze the profilometer data.

2.4 Analysis and characterization

To assess the general nature of impact events in metals, Johnson [26] used a dimensionless parameter ($\rho V / \sigma_{yd}$), where the yield stress σ_{yd} is considered to be a dynamic value. If the parameter is less than 10^{-6}, the contact is predominately elastic, whereas in the range of 10^{-3} - 10^{-1} quasi-static plasticity prevails. In this work the parameter has values in the order of $\sim10^2$. For the current impact velocity range of 45-115 m/s, it can be concluded that the event is dominated by plastic deformation.

Fig 3 shows a typical oblique impact event for a sphere. The focus of characterization and damage analysis in this study is in these regions, in addition to a comprehensive analysis of wear related phenomena. High deformation rate characterization of the studied steels is also provided to understand the dynamic stress-strain response of the investigated materials in HVPI experiments.
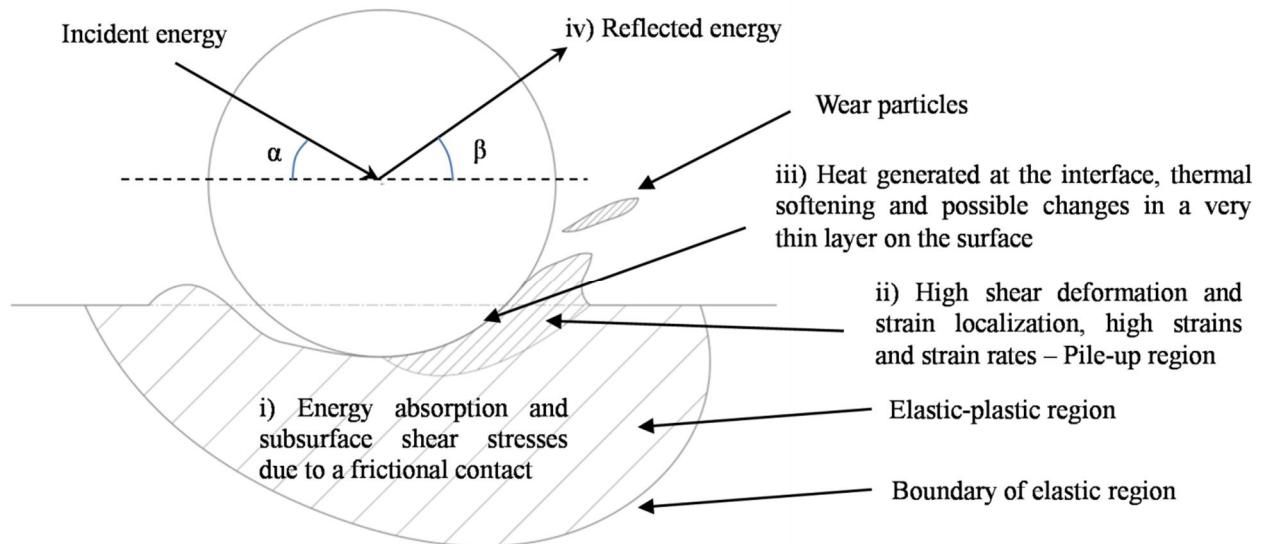
Figure 3. Deformation produced by a sphere impacting on a semi-infinite steel plate.

The impact resistance of a material can be assessed by its ability to absorb energy during an impact and by the amount of consequent material loss. The impact resistance depends on several parameters, such as the strength (e.g., hardness and elastic modulus, or their combination, i.e., the H/E-ratio) and ductility (e.g., fracture strain and strain hardening capability) of the material. In region *i)* in Fig. 3, the volume of the material undergoing elastic-plastic deformation is not quite clearly defined. However, it is important to study its ability to withstand different stress states, especially shear stresses under an oblique impact. In addition to the post impact characterization of the deformation and damage, it is important to understand also the underlying dynamics of the impact events. This requires extensive mechanical testing of the dynamic shear, tensile and compressive properties of the test material, as well as the use of currently available numerical methods such as crystal plasticity finite elements [27], which make it possible to derive and simulate even complex stress states occurring for example during oblique impacts. The advantage of this type of an approach is that the models can be adequately verified by only simple compression tests.

The region of high plastic deformation *ii)* is strictly related to shear. Among others, Hutchings and Winter have reported shear banding and fracture in this material pile-up region after impacting of a sphere [28] and angular particles [29]. As already pointed out, adiabatic shear banding and formation of white shear bands can be expected to occur in this region in the strain rate range of our experiments. Some early studies consider this region as a volume already lost from the surface due to its susceptibility to damage. In this work the relationship between material loss and cutting in this region is presented as the ratio between the crater volume and the plastically deformed volume.

In the surface region *iii)*, friction between the particle and the target surface clearly affects the subsurface stress state. The plastic nature of the contact also implies that in addition to pure sliding between the contacting surfaces, 'ploughing' should be accounted for as well. Sundararajan and Shewmon [30], and Sundararajan [31] studied the surface deformation and friction behavior using a numerical approach and analytical models. The best fit was found with a numerical model considering a composite coefficient of friction including both sliding and ploughing terms. Additionally it was summarized that friction is a strong function of the impact velocity and incident angle α, and thus the absorbed energy and also the effects of surface strain hardening should be accounted for.

Normally the erosion rate is presented as the weight loss caused by one kilogram of impacting particles (i.e., [mg/kg]). This parameter is useful for general comparison of the wear test results. The energy absorption *iv)* is connected to several parameters during the incident. The currently used

technique for analyzing the energy dissipation allows the use of a more detailed 'wear rate' term. Since material loss is a result of the material's capability to absorb energy or to reflect it away, it is natural to present the results in the form of material loss per used energy (i.e. [mm³/J]). The use of this type of a wear rate can reveal special characteristics of the surface, taking into account, for example, the fact that frictional dissipation of energy is not always constant. Additionally, in numerical simulations this term is useful as a verification value because energy dissipation during the contact can be easily calculated, although it is not as straightforward to determine where the energy was actually consumed. However, a general impact simulation using only the kinetic energies prior and after the impact should in the sense of 'in-out' energy yield a value similar to that measured in the experiments. In contrast, the volume loss inflicted by the initial kinetic energy of a particle could be useful design-wise, since then the analytical models would only require an approximate value of the impacting particle energy. This value is usually available from the process parameters or it can be measured.

3) Results and discussion

3.1 Dynamic stress-strain behavior

Fig 4. shows the compression stress-strain curves for the studied materials. The strain rate range presented here covers a quasi-static range of 10^{-3} - 10^{-1} 1/s and a dynamic range of 700 - 3600 1/s. The individual curves were smoothed with a second order polynomial based on the plastic strain region. The plot of the backward extrapolated yield strengths (Fig 4b) shows that IRS has ~10%, AIRS ~15% and COMP ~40% higher yield strength than ABRS throughout the whole experimental strain rate range. The strain rate dependence of the yield strength can be described with two linear fits with different slopes, showing that strain rate has an increasing effect on the yield strength. This is a desired characteristic for an impact resistant material, assuming that also the overall ductility of the material remains at a reasonable level.

The strain hardening rates, defined as the slope of the stress-strain curve ($d\sigma/d\varepsilon$), clearly show that the martensitic steels undergo first moderate strain hardening, after which strain softening is observed. The strain hardening is actually quite strong during quasi-static compression, but as the strain rate increases, the strain hardening decreases. The quasi-static stress-strain curves at the strain rate of 10^{-3} exceed the dynamic stress-strain curves at higher strains. Some of the quasi-static stress-strain curves were cut off in Fig 4 for illustrative purposes, but no strain softening was encountered even at higher values of strain. The temperature rise was evaluated assuming adiabatic conditions and making use of the equation $\Delta T = \beta/\rho c \int \sigma d\varepsilon$, where β is the fraction of work transformed to heat (usually between 0.9-1.0). According to this equation and $\beta = 0.95$, the bulk temperature increases by approximately 115 degrees from RT for the IRS steel in a compression test at 3600 1/s. This rather small increase in temperature cannot explain the large softening behavior of the martensitic steels, which points to local deformation mechanisms taking over. For example increasing localization of shear deformation into adiabatic shear bands can explain the rapid change of the strain hardening rate with increasing strain. The negative strain hardening rate, i.e., strain softening, was confirmed with additional tests at 4200 1/s. In the ABRS alloy this kind of strain softening was observed already at 2400 1/s.
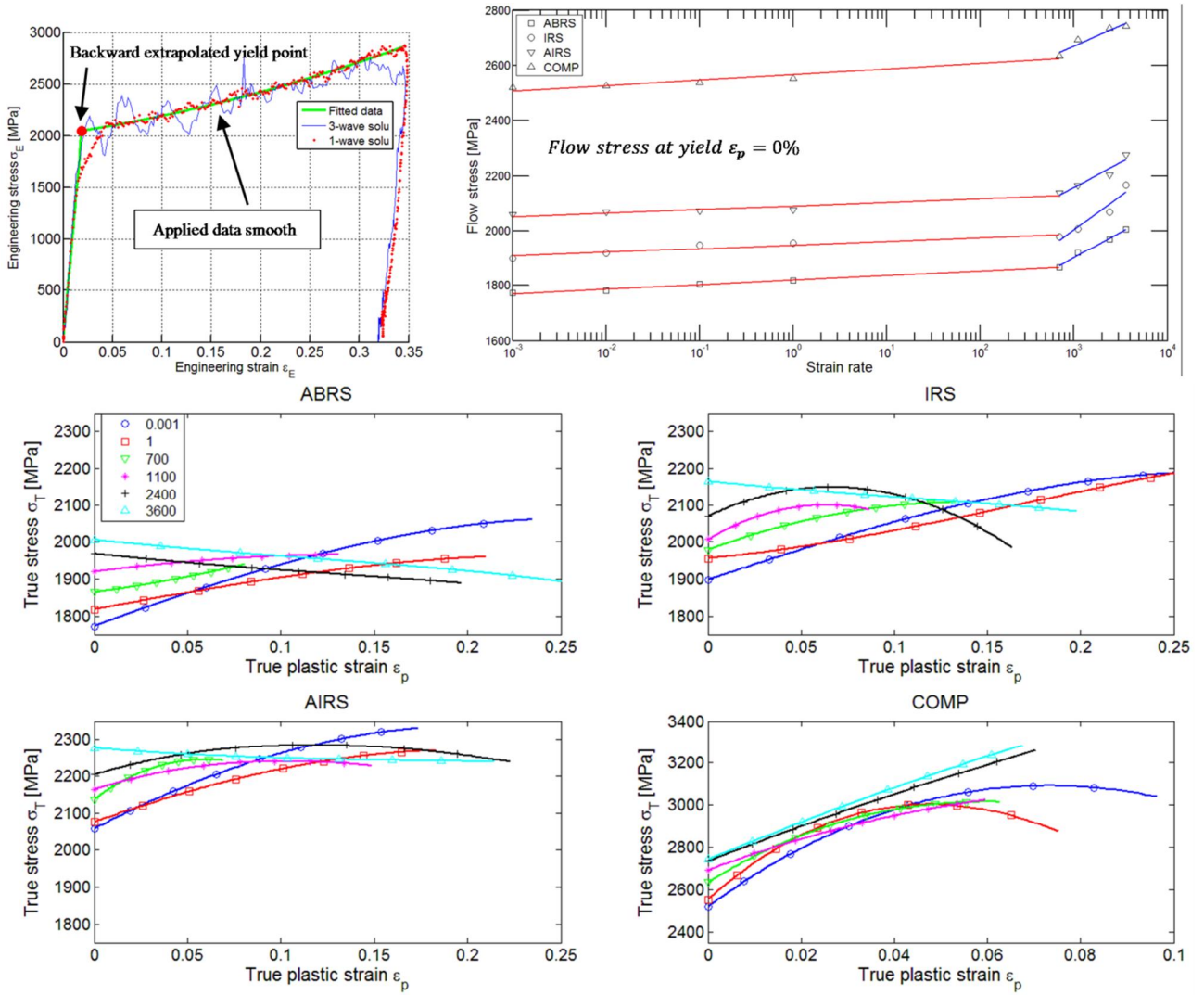
Figure 4. Mechanical behavior of wear resistant steels at different strain rates in compression.

Generally it can be observed that despite the evident strain rate dependence of strain hardening, the studied steels cannot be considered as highly strain rate sensitive materials. When comparing the yield stresses of IRS at the strain rates of 10^{-3} and 3600 1/s, we can see that the increase is only about 15%. However, during the impact events when the strain rates are extensively high, the shear banding or some other active softening mechanism may lead to failure that appears as a formation of large wear particles.

Fig 4. shows also the compression curves for the carbide reinforced steel. The brittle behavior typical to this kind of materials can be observed at the high strain rates, the maximum strains in the curves representing the failure strains of the samples. Only samples plastically strained less than 5% did not break in the high strain rate tests. When the strain rate remained below 10^0 1/s, the material did not fail in the current tests. Above 10^0 1/s the failure strain decreased clearly with increasing strain rate.

The observed adiabatic shear bands seem to play an important role in the current metal matrix composite material. The rather small reinforcing particle size [32] (~5-15um) in the material is found to affect the formation of white ASBs, while the high aspect ratio of the reinforcing particles [33] has a strain hardening effect. The onset of instability that leads to adiabatic shear banding results from the competition between strain hardening, strain rate dependent hardening, and thermal softening, which can be further complicated by local strain gradients [34] caused by the inhomogeneous distribution of carbides and the small particle size [35].

3.2 Impact deformation and wear

The impact craters were characterized quantitatively utilizing the optical profilometry data. For better understanding of the deformation at different incident energies and angles, a typical 2D profile is illustrated in Fig 5a. It is obvious that with an oblique angle impact the type of deformation and size and shape of the crater depend on the impact angle. Also the type of energy dissipation depends on the angle of impact, as the energy is consumed primarily on either deformation or cutting. Neilson and Gilchrist [36] analytically modeled solid particle erosion by an additive decomposition of the wear components. Their approach includes the normal direction component of wear due to the energy consumed on deformation and damage. The second part accounts for the kinetic energy that is parallel to the surface and is consumed on cutting of the material. The nature of the normal direction deformation is compressive under the indenting particles. However, in terms of cutting, the deformation and wear first occur by ploughing in front of the indenting particle, followed by intense shearing of the deformed material producing loose wear particles. The depth of the crater increases when the particle has more energy for normal direction deformation. The ratio between the maximum depth of the crater and the highest point of the pile-up ($R_\alpha = d_{max} / h_{max}$) shows that an increase in the angle is not always followed by a higher value of R_α. At 30 degree impact angle, R_α comes much closer to unity. For example at 17J impact energy the ratios are $R_{15} = \sim1.9$, $R_{30} = \sim1.5$, and $R_{60} = \sim2.3$ for the IRS material. Similar behavior was found for all studied materials. The lower ratio R_α indicates that a 30 degree impact creates a large pile-up around the crater. Also, it is clear that there are differences between the steels regarding this ratio. Fig 5b shows a comparison of the steels at constant impact angles and energies.
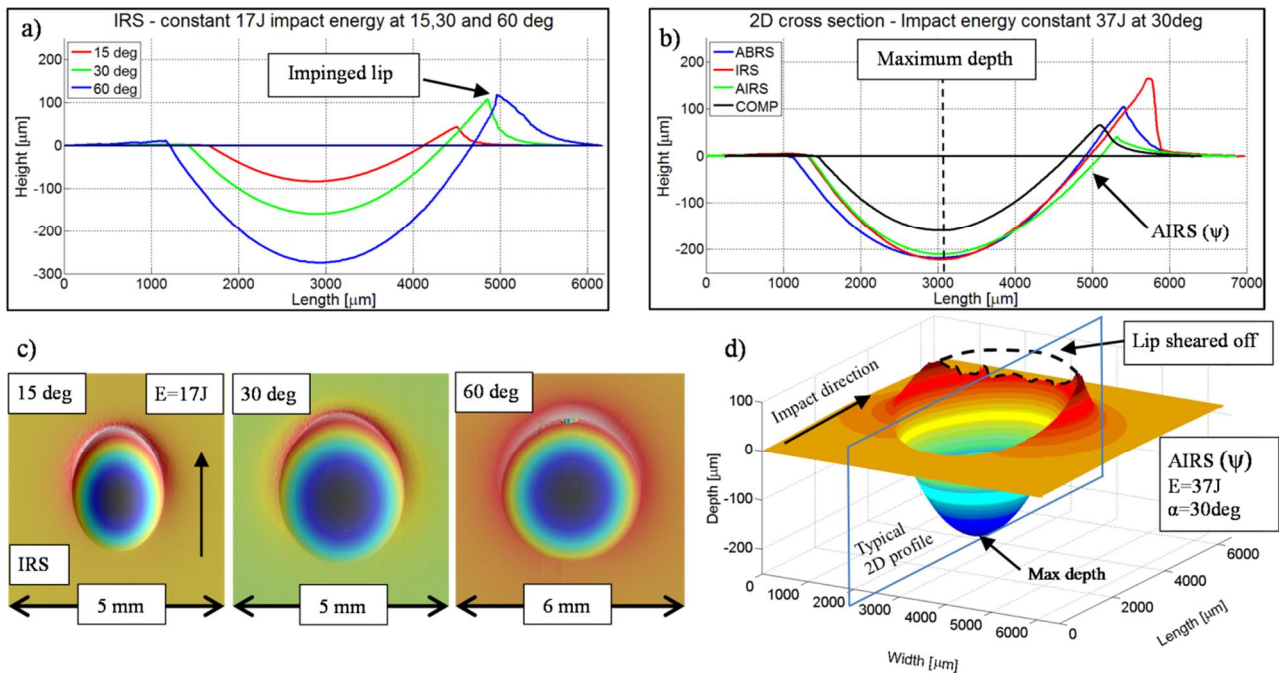

Figure 5. Deformation in a single particle impact

Part of the pile-up may also be cut off, as illustrated in a typical 3D profile in Fig 5d. The highest point then does not give enough information about the whole pile-up region. Therefore, a better estimate than the ratio R_α between cutting and plastic deformation may be simply written as

$$\varphi = \frac{|V_{neg}| - |V_{pos}|}{|V_{neg}|} \qquad (3)$$

where V_{neg} is the 'negative' volume below the zero level, and V_{pos} is the 'positive' volume above the zero level. When the value reaches 1, all material has been cut off, while 0 means that the material has been only ploughed to ridges by plastic deformation. A similar plasticity index calculated from two-dimensional values has been used to study the scratch behavior and abrasion by Zum-Gahr [4]. In the current work the three-dimensional data is better suited because of the irregular shapes of the pile-up region and the crater. As expected, the results show that the depth has a strong dependence on the impact angle and also on the impact energy. All martensitic steels show similar depth values, but the carbide reinforced COMP clearly has shallower craters.

Fig 6 shows some of the wear characteristics of the studied materials. It is evident that the volume loss has quite a strong dependence on the impact velocity (Fig 6a). On the other hand, the shape of the curve (Fig 6b) of lost volume per unit incident energy remains quite flat at different impact velocities, especially at low impact angles. The highest impact angle (60 deg) has the greatest effect on the behavior of ABRS and COMP materials, which can be explained by their increasingly high cutting ratio (Fig 6c). The low wear rate per the input energy of the IRS and AIRS materials, in turn, is a result of the greater plasticity of these materials.

The carbide reinforced steel exhibits the lowest volume loss at low angles throughout the tested impact energy range. It has the highest dynamic yield strength and is therefore capable of absorbing a lot of energy during the impact as long as the energy remains at a reasonable level. However, as the fracture strains in the dynamic range are relatively small even in compression, the microstructure cannot accommodate much of the energy by plastic deformation, which leads to fracturing of the material at higher impact angles. The result is very common for hard and relatively brittle metal matrix composites, which are not generally good against normal direction impacts. The COMP material showed a large subsurface crack network already at 60 degrees with 17J impact energy.
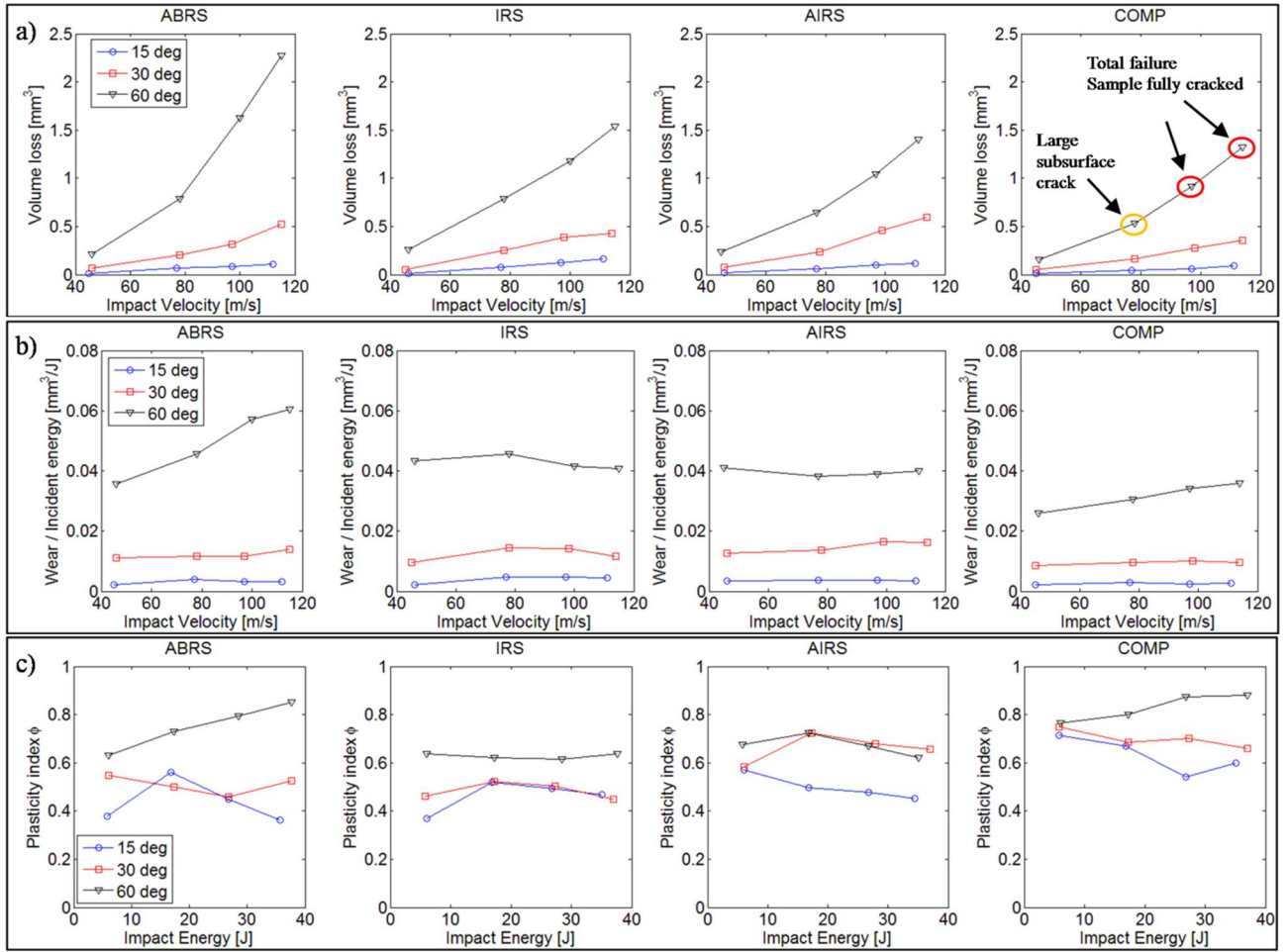
Figure 6. a) Material volume loss at different impact velocities, b) wear rate as volume loss per incident energy at different impact velocities, c) cutting-to-plasticity ratios at different angles.

3.3 Damage characterization

Fig 7. shows cross-sectional images of the high strain rate compression samples tested at 3300-3600 1/s. The images are from the middle of the sample along the x_1-x_3 plane depicted schematically in Fig 7a.
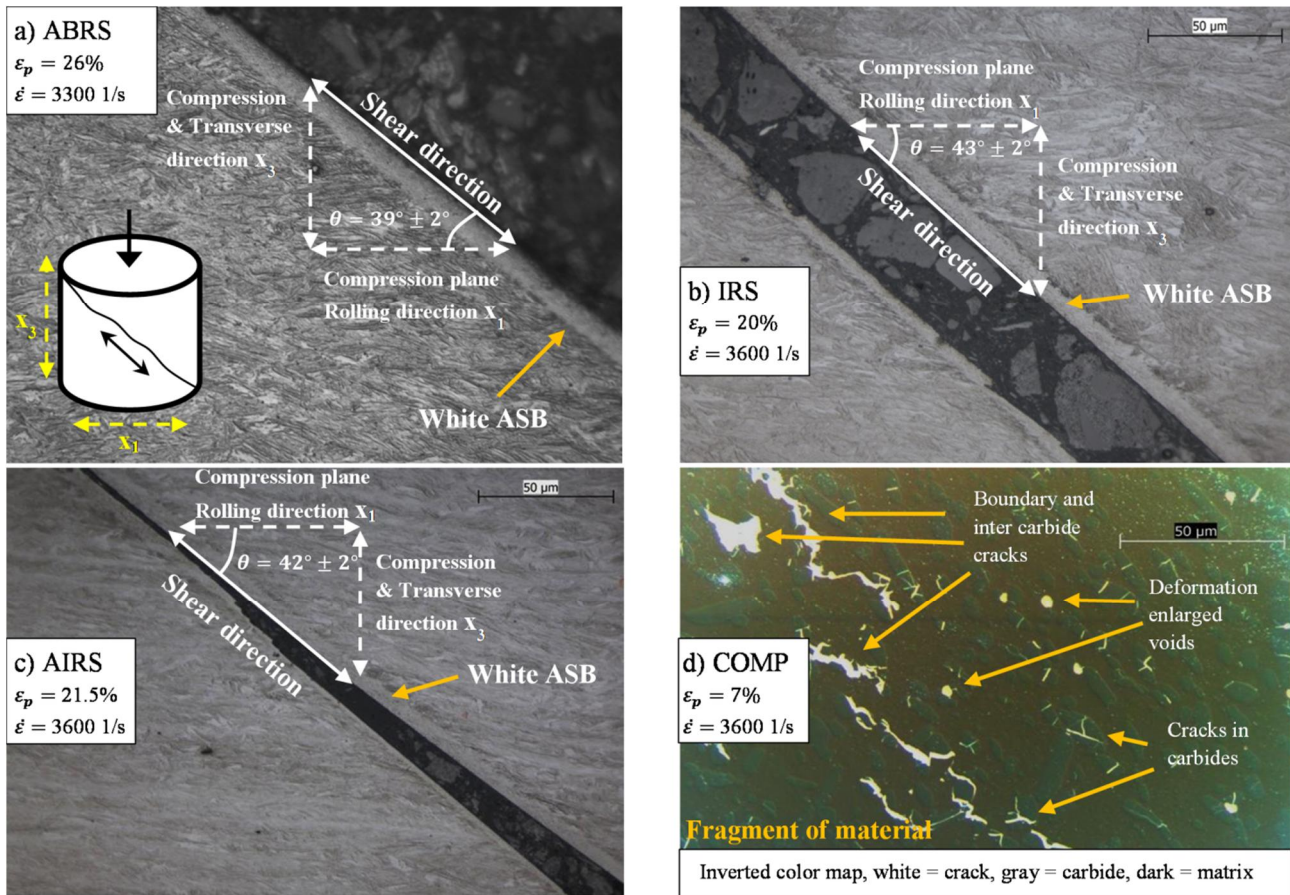
Figure 7. Shear failures and damage in high strain rate compression samples.

The martensitic steels exhibited typical shear failure into two or a few pieces, while the carbide reinforced steel samples fractured into several smaller pieces. The martensitic steels failed typically by fractures initiating within a white adiabatic shear band. A comparison of the two failed halves of an IRS sample shows that both sides contain a white shear band layer on the fracture surface, indicating that the fracture occurred inside the shear band and not along the interface between the untransformed material and the shear band. The axial plastic strain at failure was typically over 20%. A study on the lower strain rate samples, which did not fail even at high strains, and on the failed and unfailed high strain rate samples confirmed that in these materials fracture takes place only when white shear bands are present.

ABRS required the highest plastic strain to fracture. At strain levels around 20%, AIRS with the highest strength had a tendency to ASB formation and fracture, while ABRS showed the least fractured samples. This suggests that ABRS has a relatively ductile microstructure, which may result from the absence or a low amount of bainite in the microstructure. Table 3 shows the measured microhardness values from the deformed and fractured samples. ABRS does not undergo such high strain hardening, which is observed with IRS and AIRS. Retained austenite is known to have an effect on the strain hardening and ductility of martensitic steels [37,38,39], but since the studied steels contain approximately only less than 1% of retained austenite, it is not likely to have a marked effect on their hardening behavior. On the other hand, due to the self-tempering process taking place during the manufacturing and the different alloying, the amounts of untempered martensite in the microstructure are very likely to have an effect, as suggested by the higher hardness values of IRS and AIRS. The highest increase in hardness due to strain hardening was observed for IRS, close to 40% from the bulk hardness.

Table 3. HV0.025 Microhardness values of the steels after compression to failure occuring at ca. 20 %.

Material	Undeformed steel	Deformed steel	Shear band
ABRS	511 ± 8	600 ± 12 (19 %)	741 ± 5 (43 %)
IRS	517 ± 9	707 ± 8 (37 %)	796 ± 14 (54 %)
AIRS	542 ± 7	724 ± 10 (34 %)	824 ± 8 (52 %)
	Undeformed matrix	Deformed matrix	Carbides
COMP	739 ± 18	848 ± 12 (15 %)	1385 ± 107

·   (x-%) – Mean value of the increase of hardness from bulk hardness

Microhardness measurements of the white shear bands showed that their hardness was clearly higher than that of the surrounding matrix. For example Odeshi et al. [40], who studied the shear bands in AISI 4340 after impact with a Hopkinson bar, found that the hardness values in a white shear band were almost twice the bulk hardness. They also concluded that the surrounding matrix does not undergo severe strain hardening even at failure, which leaves the matrix hardness values rather low. Although AISI 4340 is very similar to the current alloys, it is evident from Table 3 that plenty of strain energy has been stored in the matrix of these materials as well.

Odeshi and Bassim [41] reported post-impact hardness values also for DP-steels, which showed significant strain hardening capability of the matrix almost up to the same level as the martensitic steels, even when shear bands were present. Their results suggest that it is important that the steel is capable of homogenous deformation so that localization that leads to failure may not immediately take place in impact conditions. Lee et al. [42], in turn, investigated adiabatic shear banding in carbon steels using hat shaped samples. The studied carbon steels mostly developed deformed bands, which showed reasonable increase in hardness. When both deformed and transformed bands were found in the steel, the hardness values were remarkably higher, as found also in the current work. In a Hopkinson Split Bar study [43] on the effects of tempering temperature on the adiabatic shear banding of AISI 4340, different fracture modes were found. The authors explain that the observed fracture behavior controlled by the adiabatic shear bands is generally a result of void initiation and growth due to thermal softening.

The characteristic failure and damage mechanisms in the carbide reinforced steel COMP are illustrated in Fig 10, which shows that the principal fracture paths are mainly in the matrix but carbides fracture as well. Reasonable amounts of cracked carbides were found even away from the main fracture bands. Also adiabatic shear bands may be present in the microstructure. Table 3 shows that the initial hardness of the tempered martensitic matrix is quite high and that the amount of strain hardening before fracture is rather limited.
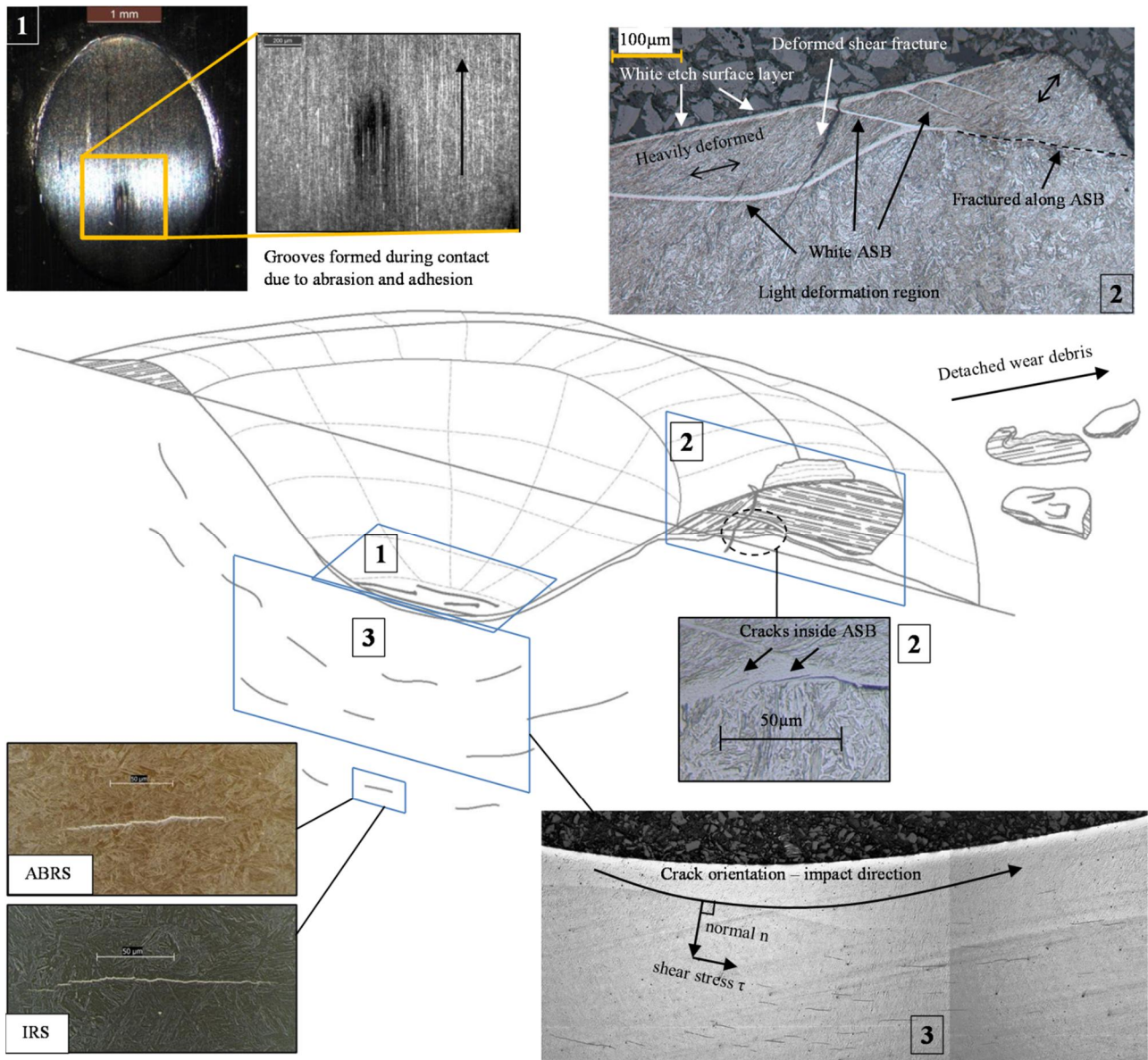
Figure 8. Schematic of impact damage, deformation and wear in HSLA steels.

Fig 8 demonstrates the damage mechanisms prevailing in the studied martensitic high strength steels during an oblique impact. In a cross sectional study of the crater, several different mechanisms can be identified: 1. the crater bottom shows signs of adhesion and abrasion due to small particles detached from the surface; 2. the most important region in terms of wear is the pile-up region, which exhibits heavy shear deformation and both deformed and transformed (white) adiabatic shear bands. Also a clear white layer roughly ~10µm in thickness is formed on the surface. The failure in the white adiabatic shear bands shows similar initiation and propagation behavior as observed by Bassim and Odeshi [44], i.e., micro-voids initiating inside the ASBs and then forming clusters elongated parallel to the shear band. The clustered voids further lead to the forming of micro cracks, which eventually interconnect to form larger fracture patterns responsible for the fragmentation of the material along the shear band; 3. subsurface cracks with lengths varying from tens to hundreds of micrometers occurring at various depths.

*AVG-SB is the average value of five additional hardness points in a white shear band
*AVG-SL is the average value of five additional hardness points in the white surface layer
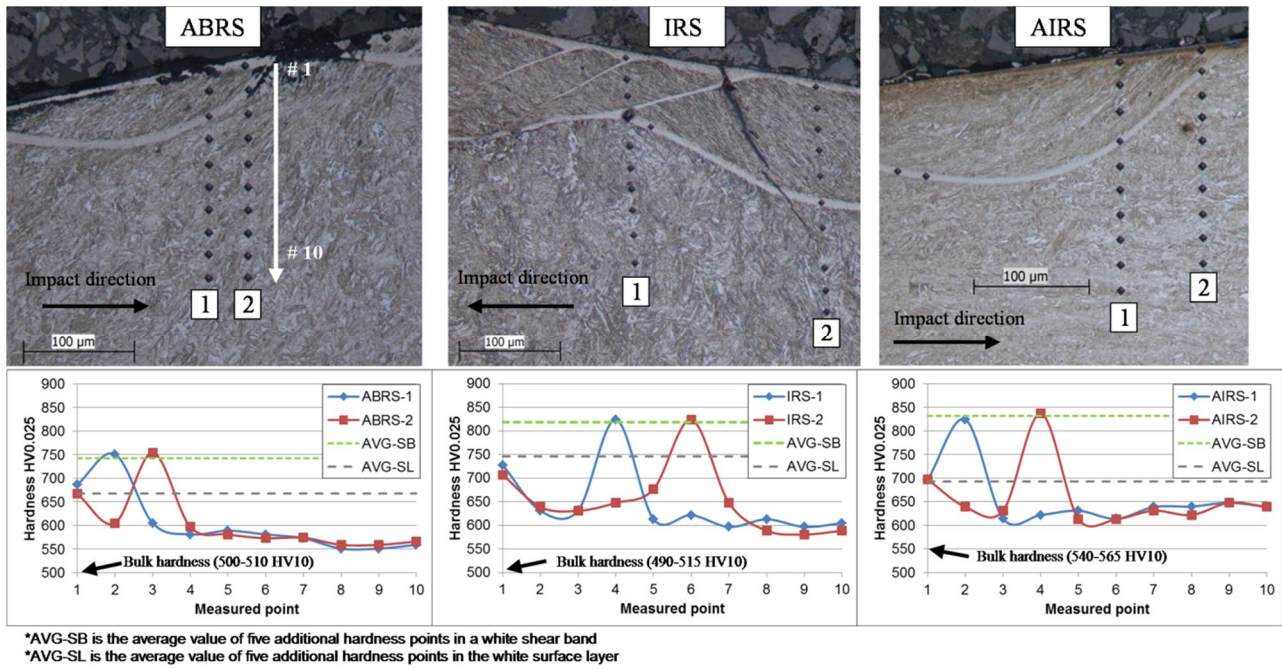
Figure. 9. Cross-sectional microhardness profiles measured from the white surface layer, white shear bands and deformed matrix of HSLA steels produced in a single impact at 30 degrees.

The microhardness measurements performed on the white surface layers, deformed shear band regions, and the white shear bands of the HVPI samples reveal strain hardening behavior similar to that observed in the compression tests. As seen in Figure 9, the white surface layer has a mean hardness that is less than the mean hardness of the subsurface white shear bands. The observed behavior could be due to some differences in the microstructure and/or boundary conditions during the formation of the shear bands. For example, it is likely that heat is conducted slower away from the surface layer than from the shear band completely surrounded by the cold matrix metal, which may lead to partial tempering of the microstructure of the white surface layer. Also, the stress state of an internal white shear band is supposedly different because of the surrounding matrix compared with the free outer surface. The hardness of the internal white shear bands is in good agreement with the values measured from the compression test samples. Since the strain rate is obviously higher in the impact tests, the slightly higher hardness values suggest also a small dependence of shear band formation on the strain rate. In fact, Bassim and Odeshi [44] also observed strain rate dependent hardness of the white ASBs.
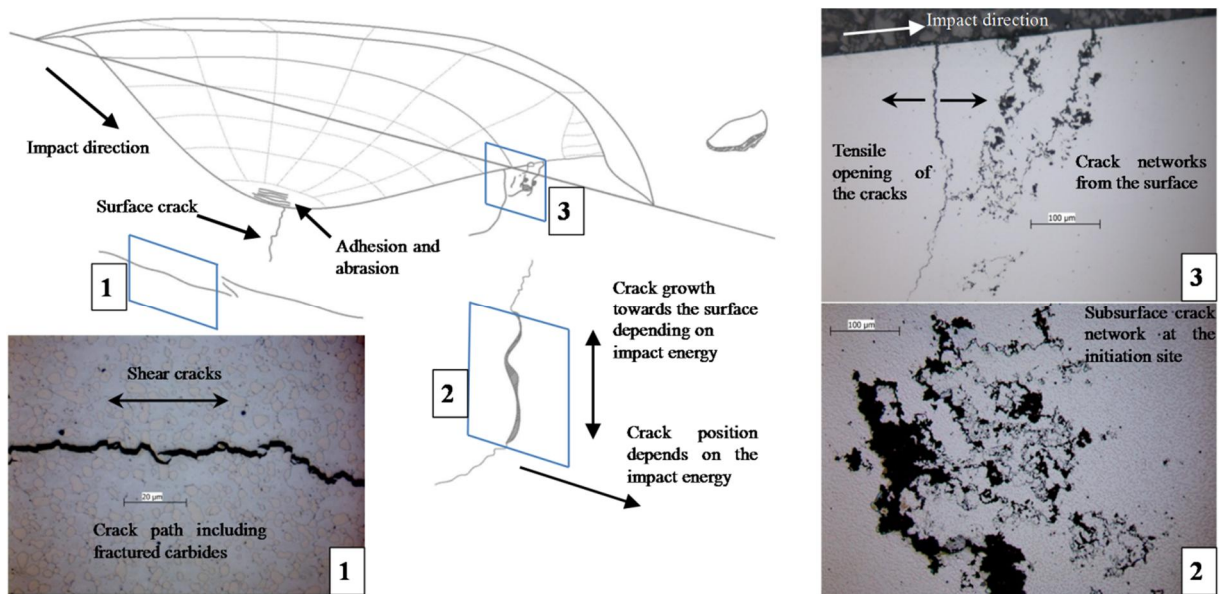
Figure 10. Damage characterization of a carbide reinforced steel (COMP) sample after a 30 degree impact.

The impact damage in the carbide reinforced steel is different from the fully martensitic steels studied in this work. Fig 10 illustrates the damage and failure behavior of COMP at high strain rates and high impact energies (27J and 37J) in tests conducted at an impact angle of 30 degrees. The high hardness to modulus ratio (H/E) would indicate a good energy absorption capability for the steel, but as shown by the mechanical testing results, the martensitic matrix does not have a good enough strain hardening capability at large elongations. The cracks in the carbides may also act as initiation sites for the cracks in the matrix, as seen in Fig 7. Reasonable amounts of cracked carbides were found even away from the main fracture bands.

One of the common damage types observed in the cross sections of the impact craters are the subsurface lateral cracks (1). The bottoms of the craters also show clear signs of adhesion and abrasion, most likely by the detaching carbides dragging along the surface. Small secondary fractures along the carbide-matrix boundaries were detected right on the surface by optical inspection. This explains the detachment of the carbides during the frictional contact between the impacting particle and the steel surface.

A large subsurface crack network was found perpendicular to the surface (2). An increase in the impact energy increased the length of the cracks first observed at the impact energy of 17J. At the highest impact energy of 37J at an impact angle of 30 degrees, the fracture had propagated all the way to the top surface and almost through the whole sample thickness. The location of the crack network was found to depend on the impact energy, which probably is due to the different subsurface stress fields during the impact. Near the pile-up region a surface crack network was observed, which was probably first initiated by the compressive stresses and then grown due to the tensile stresses acting after the particle had passed the area.
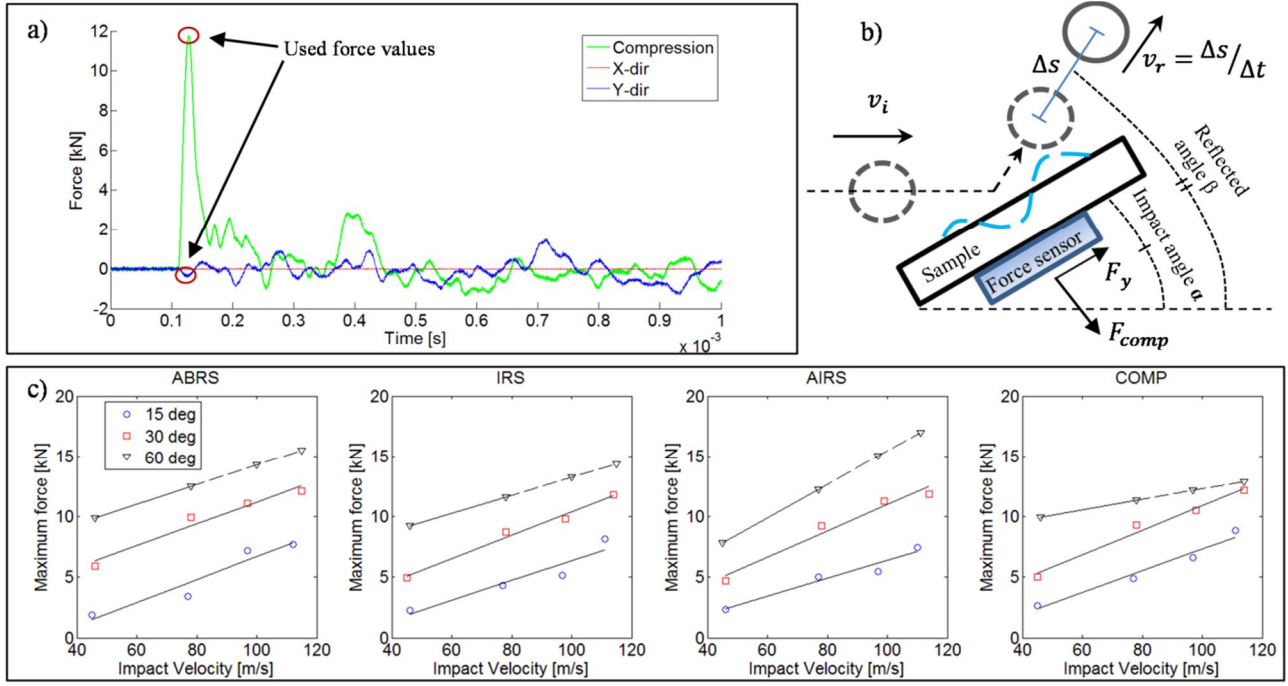
Figure 11. a) Force measurements during a 30 degree impact at 114 m/s, b) a schematic of the impact event and the energy calculations, c) the measured maximum force values and linear fits to the data points

Fig 11a shows the contact forces as a function of time during a 30 degree impact at 114 m/s. The force sensor, which was located directly below the impact crater, recorded the highest forces F_{comp} in the compression direction, while the vertical sliding forces F_y did not reach very high values. As expected, the F_x forces in the sideways direction were essentially zero throughout the impact. The maximum resultant force was calculated using equation 4.

$$F_{max} = \sqrt{F_{comp}^2 + F_y^2} \tag{4}$$

In the illustrated case, the first compression force spike lasts only 50 microseconds, which could be roughly confirmed from the high speed photography to be the contact time. The maximum force values observed for different materials are consistent for 15 and 30 degree impact angles. The 60 degree values may not be as reliable because the forces were close to the upper limits of the sensor. Therefore at the highest impact energies the 60 degree values were extrapolated from the lower velocity data, as shown with the dashed lines in Figure 11c. Overall, the correlation between impact energy and maximum force seems to be quite linear.

Fig 12a shows the reflection angle as a function of impact velocity for 15 and 30 degree incident angles. The reflection angle at the 60 degree incident angle could not be measured with the current test setup due to a high reflection angle close to 90 degrees. The reflection angle β was measured as an absolute angle from the horizontal direction, as shown in Fig 11.
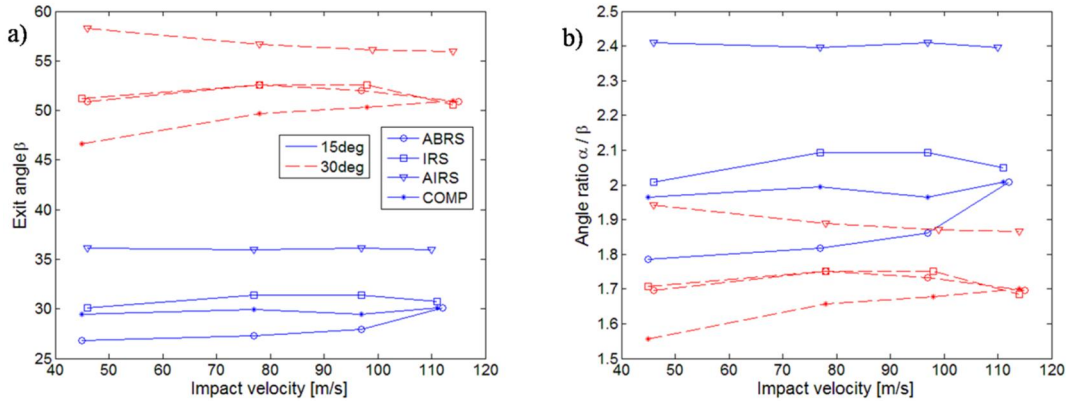
Figure 12. a) Measured reflected angles for 15 and 30 degree impacts and b) ratios between incident and reflected angles.

The reflected angle shows a clear material dependence, as seen in Figure 13. At 15 and 30 degree incident angles, the reflected angles vary between 27 and 37 degrees and 47 and 58 degrees, respectively. The angle ratios in Figure 13b show more clearly also the effect of velocity. For the martensitic alloys, the differences between the grades as well as the velocity dependence of the reflected angle could be explained by the changes in the ratio of cutting and deformation as a mechanism of material removal or displacement. Also in the composite steel similar behavior was observed: when plasticity increases in the pile-up region (Fig 6c), the reflected angle becomes slightly larger.

Figure 13 shows a summary of the wear rates for the materials studied in this work as a function of impact angle and impact energy. The wear mapping, i.e, the wear regions indicated in the plots, is based on the failure mechanisms observed in the characterization of the wear surfaces and sample cross-sections. The wear rates in the plots are presented as volume loss per dissipated energy. The fraction of the incident energy spent in the contact, i.e., the dissipated energy, varies slightly between the tested materials. On the other hand, the dissipated energy is a strong function of the incident (impact) angle, ranging between 13-21%, 33-44% and 80-82% for the impacts at 15, 30 and 60 degree angles, respectively.
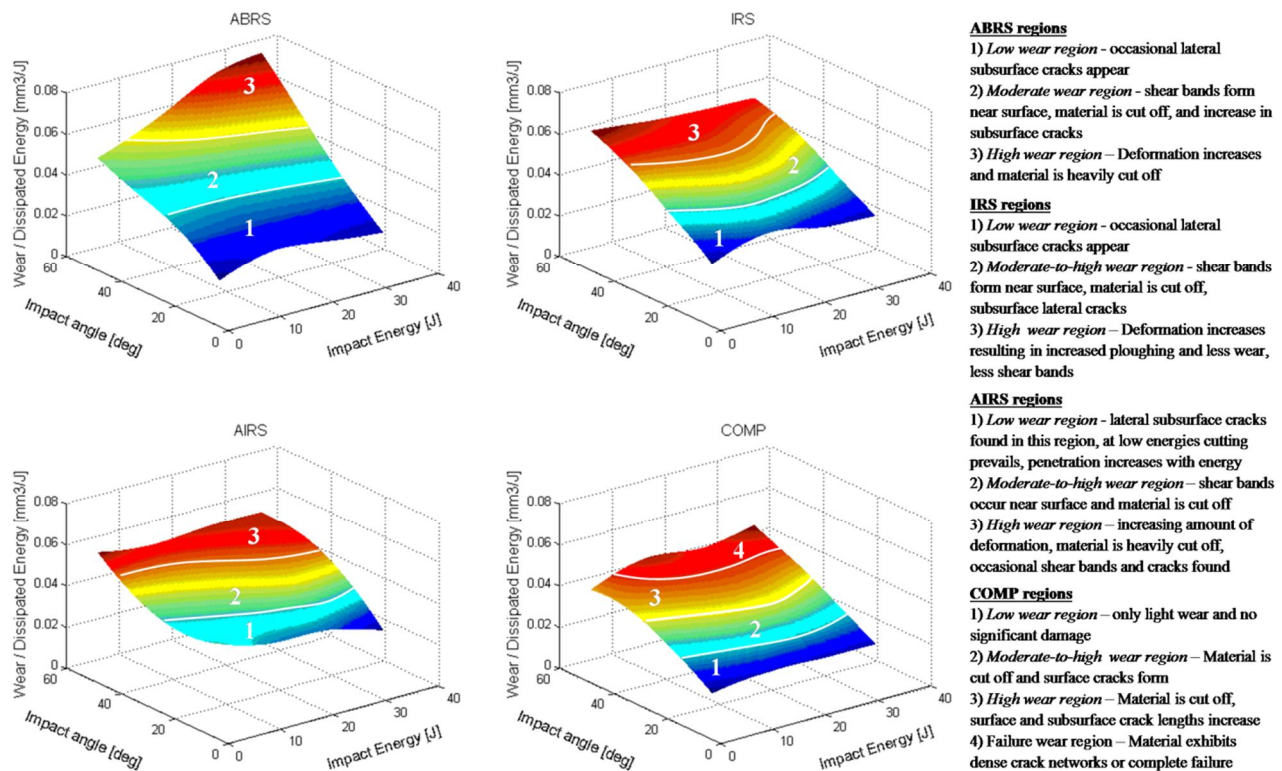
Figure 13. Summary of wear the rates, wear mechanisms, and damage based on the characterization of single particle impact samples at angles between 15-60 degrees.

For the high strength martensitic steels, three characteristic wear regions could be distinguished. The first region was identified as a *low wear region,* where a simple cutting mechanism prevails. In the *moderate-to-high wear region*, the steels generally exhibit severe shear banding and fracture initiation in the shear bands. In addition, there were clear signs of subsurface shear cracking, which under continued impacting may accelerate wear by fatigue fracture. The *high wear region* was mostly observed at high impact angles. Based on the observations, large parts of the ploughed ridges had been cut off, perhaps along the adiabatic shear bands since the white surface layer was found also at high angles.

For the carbide reinforced steel, the first region was similar to that of the martensitic steels, i.e., a low wear region. Material is worn mainly by cutting, but the transition to the moderate wear region is likely due to two factors. Firstly, increasing of the impact energy at higher angles causes crack formation due to the exhaustion of the mechanical strength and energy absorption capability of the matrix and the carbides. Secondly, the increased strain rate was observed to activate dynamic failure mechanisms further promoting crack initiation, which may be connected to the shear localization in the adiabatic shear bands in the matrix. In the high wear rate region subsurface and surface cracks are observed more intensively and cutting of the material increases. Finally a region where this material is not any more usable was found at high impact angles and high energies. In this region the material fails catastrophically even by a single impact.

4) Summary and Conclusions

An experimental high strain rate impact study was carried out on four high strength wear resistant steels. The mechanical behavior of the studied materials was first established using quasi-static and high strain rate compression tests. The high strain rate samples were characterized to identify the prevailing damage and failure mechanisms. High velocity impact testing was executed with a novel

high velocity particle impactor (HVPI) using large sized (9 mm) spherical particles at various impact angles, speeds and energies. A comprehensive post impact analysis of the craters was performed to characterize the mechanical response and wear behavior of the studied steels. Based on the obtained results, the following conclusions may be drawn:

1) The high strength martensitic steels exhibit strain softening at high strain rates and relatively large strains. The shear localization can occur when nearly adiabatic conditions prevail during the deformation. The main failure mechanism in the compression tests was identified as fracturing along white shear bands. The common increase in the yield stress was observed with increasing strain rates.

2) In the high strain rate tests the chromium carbide reinforced metal matrix composite experienced more or less complete fragmentation before reaching ca. 8% of plastic strain. The fracture strain was observed to somewhat depend on the strain rate below 2400 1/s.

3) The total amount of strain hardening before fracture was evaluated using microhardness measurements. The increase in the hardness of the deformed martensitic steel matrix varied from 19% to 34%. The hardness in the white shear bands was, in turn, 43% - 52% higher than that of the undeformed matrix. The initially hard martensitic matrix of the composite steel hardened only by ~15%.

4) Cutting was found to be the prevailing mechanism of wear at the impact angle of 15 degrees. The role of plastic deformation increased pronouncedly in the formation of the crater at the 30 degree impact angle. In contrast to the general expectation that the highest wear rates of steels occur at low angles, the amount of wear reached a maximum at 60 degrees due to combined heavy deformation and cutting. However, the adiabatic shear bands showed signs of crack initiation that may under continued impacts lead to higher wear rates also at 30 degrees.

5) Deformed and transformed shear bands were found as the prevailing damage and failure mechanism in the pile-up region especially at high impact velocities for the martensitic steels. Subsurface shear cracking parallel to the trajectory of the projectile was also observed. This behavior may be explained by the subsurface shear stress maxima, the location of which depends on the momentary position of the sliding particle in the forming impact crater. Numerical simulations of the impact events might explain the evolution of the stress state in more detail. A thin and hard white surface layer was observed in the cross sections, but its detailed relationship to wear was not further studied in this work.

6) The carbide reinforced steel exhibited cutting at low impact angles with relative low wear rates. At 30 degrees fracture initiation leading to networks was found to increase as a function of the impact energy and strain rate. The adiabatic shear banding may contribute to the cracking by allowing large deformations and by facilitating brittle fracture initiating from the defects. The 60 degree impact angle is extremely challenging for the material in the current impact energy range, and the material quickly reaches its limit for imminent catastrophic failure.

7) Despite the apparent differences between the high velocity impact and the high strain rate mechanical testing, the cross sectional characterization of the test samples showed that identical failure/wear mechanisms were active in both cases. This confirms the suitability of the used HVPI test setup for high velocity impact testing as a verification tool for actual impact conditions.

8) The amount of energy consumed during deformation was found to be material dependent and related to, among other things, friction and mechanical properties of the test material. In general, however, the consumed energy was found to depend strongly on the incident angle of the impact event.

Acknowledgements

References

[1] Ratia, V., Miettunen, I., Kuokkala, V-T., Surface deformation of steels in impact-abrasion: The effect of sample angle and test duration. Wear 301(2013), pp.94-101.

[2] Johnson, K.L. Contact Mechanics, Cambridge University Press, 1985.

[3] Engel, P.A., Impact Wear of Materials, Tribology Series, 2, Elsevier Scientific Publishing Company, 1978.

[4] Zum-Gahr, K.H. Microstructure and wear of materials. Tribology Series 10, 1987 Elsevier.

[5] Levy, A.V. Solid particle erosion and Erosion-Corrosion of Materials. ASM International, 1997, Second edition.

[6] Kleis, I., Priit, K. Solid particle erosion – Occurrence, Predition and Control. Springer-Verlag, 2008.

[7] Zener, L., Hollomon, J. H. , Effect of strain rate upon plastic flow of steel, Journal of Applied Physics, 15(1944)1, pp. 22-32.

[8] Duan, Z. Q., Li., S. X., Huang, W., Microstructures and adiabatic shear bands formed by ballistic impact in steels and tungsten alloys. Fatigue & Fracture of Engineering Materials & Structures, 26(2003)12, pp. 1119-1126.

[9] Chen, Z.H., Chan, L.C., Lee, T.C., Tang, C.Y. An investigatino of formation and propagation of shear band in fine-blanking process. Journal of Materials Processing Technology, 138(1003), pp.610-614.

[10] Murr, L.E., Ramirez, A.C., Gaytan, S.M., Lopez, M.I., Martinez, E.Y., Hernandez, E., Martinez, E. Microstruture evolution associated with adiabatic shear bands and shear band failure in ballistic plug formatino in Ti-6Al-4V targets, Materials Science and Engineering A, 516(2009), pp. 205-216.

[11] Xin, Z.X., Ma, C.M., Li, S.X., Cheng, G,Q. Perforation of an ultra-high strength steel penetrated by shaped charge jet. Materials Science and Engineering A, 379(2004), pp.443-447.

[12] Atapek, S.H., Karagoz, S. Ballistic impact behavior of a tempered bainitic steel against 7.62 mm armour piercing projectile. Defence Science Journal, 61(2011), pp.81-87.

[13] Dodd, B., Bai, Y. Adiabatic shear localization. Elsevier Ltd. 2012.

[14] Finnie, I. Erosion of surfaces by solid particles. Wear, 3(1960), pp. 87-103.

[15] Bitter, J.G.A, A study of erosion phenomena, part I, Wear, 6(1963), pp. 5-21.

[16] Bitter, J.G.A, A study of erosion phenomena, part II, Wear, 6(1963), pp.169-190.

[17] Meng, H.C., Ludema, K.C., Wear models and predictive equations: Their form and content. Wear, 181-183(1995), pp.443-457.

[18] Oka, Y.I., Ohnogi, H., Hosokawa, T., Matsumara, M. The impact angle dependence of erosion damage caused by solid particle impact. Wear, 203-204(1997), pp.573-579.

[19] Sheldon, G. L., Similarities and differences in the erosion behavior of materials. Journal of Basic Engineering, Transaction of ASME, 9(1970), pp. 619-626.

[20] Apostol M., Kuokkala, V-T., Laukkanen, A., Holmberg, K., Waudby, R., Lindroos, M. High velocity particle impactor – Modeling and experimental verification of impact wear test. World Tribology Congress WTC 2013, Turin, Italy Sept 8-13. 2013.

[21] Apostol, M., Vuoristo, T., Kuokkala, V-T. High temperature high strain rate testing with a compressive SHPB. Journal de physique IV, 110(2003), pp. 459-464.

[22] Gorham, D.A., A numerical method for the correction of dispersion in pressure bar signals, Journal of Physics Part E: Scientific Instruments, 16(1983), pp.477-479.

[23] Sarlin, E., Apostol, M., Lindroos, M., Kuokkala, V.-T., Vuorinen, J., Lepistö, T., Vippola, M. Impact properties of novel corrosion resistant hybrid structures, Composite structures 108(2014), pp.886-893.

[24] Salman, A.D., Biggs, C.A., Fu, J., Angyal, I., Szabó, M., Hounslow, M.J. An experimental investigation of particle fragmentation using single particle impact studies. Powder technology 128(2006), pp.36-46.

[25] ISO standard 3290-1:2008, Rolling bearings — Balls — Part 1: Steel balls.

[26] Johnson, W. Impact strength of materials, Arnold 1972.

[27] Roters, F., Eisenlohr, P., Bieler, T.R., Raabe, D. Crystal plasticity finite elements in materials science and engineering. Wiley-VCH, 2010.

[28] Hutchings, I.M., Winter, R.E. The erosion of ductile metals by spherical particles. Journal of Physics D: Applied Physics, 8(1975), pp.8-14.

[29] Winter, R.E., Hutchings, I.M. Solid particle erosion studies using single angular particles. Wear, 29(1974), pp.181-194.

[30] Sundararajan, G. Shewmon, P. G. The oblique impact of a hard ball against ductile, semi-infinite target materials – Experiment and analysis. International Journal of Impact Engineering, 6(1987)1, pp. 3-22.

[31] Sundararajan, G. The energy absorbed during the oblique impact of a hard ball against ductile target materials. International Journal of Impact Engineering, 9(1990)3, pp. 343-358.

[32] Dai, L.H., Liu, L.F., Bai, Y.L. Effect of particle size on the formation of adiabatic shear band in particle reinforced metal matrix composites. Material Letters 58 (2004), pp. 1773-1776.

[33] Li, Y., Ramesh, K. T. Influence of particle volume fraction, shape and aspect ratio on the behavior of particle-reinforced metal-matrix composites at high rates of strain. Acta Materialia, 46(1998)16, pp. 5633-5646.

[34] Liu, L.F., Dai, L.H. Yang, G.W. Strain hardening effects on deformation strengthening behavior of particle reinforced metal matrix composites. Materials Science and Engineering A, 345(2003), pp.190-196.

[35] Dai, L.H., Liu, L.F., Bai, Y.L. Formation of adiabatic shear bands in metal matrix composites International Journal of Solids and Structures, 41(2004), pp.5979-5993.

[36] Neilson, J.H., Gilchrist, A. Erosion by a stream of solid particles. Wear 11(1968).

[37] De Moor, E., Lacroix, S., Clarke, A.J., Penning, J., Speer, J.G. Effect of retained austenite stabilized via quench and partitioning on the strain hardening of martensitic steels, Metallurgical and materials transactions A. 39(2008), pp. 2586-2595.

[38] Nakagawa, H., Miyazaki, T. Effect of retained austenite on the microstructureand mechanical properties of martensitic precipitation hardening stainless steel. Journal of Materials Science 34(1999), pp.3901-3908.

[39] Jacques, P.J., Ladrière, J., Delannay, F. On the influence of interactions between phases on the mechanical stability of retained austenite in transformation-induced plasticity multiphase steels. Metallurgical and materials transactions A. 32(2001), pp. 2759-2768.

[40] Odeshi, A.G., Bassim, M.N., Al-Ameeri, Q. Li. Dynamic shear band propagation and failure in AISI 4340 steel. Journal of Materials Processing Technology, 169(2005), pp.150-155.

[41] Evolution of adiabatic shear bands in a dual-phase steel at very high strain rates. Materials Science and Engineering A, 488(2008, pp.235-240.

[42] Adiabatic shearing behavior of different steels under extreme high shear loading. Journal of Nuclear Materials 374(2008), pp. 313.319.

[43] Odeshi, A.G., Bassim, M.N., High strain-rate fracture and failure of a high strength low alloy steel in compression. Materials Science and Engineering A, 525(2009), pp. 96-101.

[44] Bassim, M. N., Odeshi, A. G., Shear strain localization and fracture in high strength structural materials, Materials Science and Engineering, 31(2008)2, pp. 69-74.